ADVANCED FUNCTIONAL MATERIALS
www.afm-journal.d

Covalent Phenanthroline Framework Derived FeS@Fe_3C Composite Nanoparticles Embedding in N-S-Codoped Carbons as Highly Efficient Trifunctional Electrocatalysts

Fantao Kong, Xiaohong Fan, Aiguo Kong, Ziqian Zhou, Xiaoying Zhang, and Yongkui Shan**

Efficient and earth-abundant materials with multifunctional electrocatalytic properties within a wide range of pH are the new darlings for developing green energy conversion and storage techniques. A novel porous covalent phenanthroline framework (Fe-Phen-COFs) that involved Fe-DMSO (dimethyl sulfoxide) coordination complexes is successfully synthesized using 3, 8-dibromophenanthroline and 1, 3, 5-benzenetriboronicacid trivalent alcohol ester as a rigid building block via Suzuki coupling reaction. Fe-Phen-COFs as the self-carrier enriched with Fe, S, N, and C is pyrolyzed to produce N-S-codoping carbons with embedded core–shell Fe_3C and FeS composite nanostructures (FeS/Fe_3C@N-S-C). The FeS/Fe_3C@N-S-C-800 obtained by pyrolysis at 800 °C exhibits efficient trifunctional electrocatalytic activity for oxygen reduction reaction (ORR), oxygen evolution reaction (OER), and hydrogen evolution reaction (HER) within a wide pH range. Impressively, the ORR half-potential of FeS/Fe_3C@N-S-C-800 reaches 0.87 V in 0.1 M KOH, more positive than the previously reported Pt-free electrocatalysts. It could be utilized as the advanced air electrode materials in zinc–air batteries, which exhibit an excellent power density and cycling stability superior to those of Pt/C-based zinc–air battery. Thermal conversion of novel Fe-Phen-COFs provides an effective strategy to prepare high-performance trifunctional electrocatalytic materials for the new-generation powerful energy conversion technologies.

1. Introduction

Electrical splitting water into hydrogen and oxygen and recovering them in fuel cells could serve as a green and renewable energy conversion and storage technology.[1–6] The high-rate oxygen reduction or evolution reaction (ORR or OER) and hydrogen evolution reaction (HER) at lower overpotentials are of great importance to the enhancement of energy utilization rate and output power in these green energy systems. Currently, tremendous attentions have been paid on exploring low-cost nonprecious metal electrocatalysts (NPMCs) to efficiently catalyze these electrochemical processes, for completely eliminating Pt-based and Ir/Ru-based noble metal catalysts with limiting resources and time-drifting catalytic efficiency.[7–11] For minimizing the cost of the electrode catalytic layers, it is undoubtedly the most promising that a trifunctional electrocatalyst can high-efficiently catalyze the three electrocatalytic processes in one electrolyte. In the past decades, some carbon-based NPMC electrocatalysts with competitive catalytic performance have been reported by optimizing the morphologies and local structures of catalytic materials.[12–16] However, most of electrocatalysts were only efficient for a single electrochemical process.[17,18] The active ORR electrocatalyst often exhibited poor OER or HER performance and vice versa.[19,20] It is still a challenge to develop high-performance and low-cost trifunctional NPMCs.[17,21,22]

A vast range of carbon-supported nonprecious metal-based materials, including metal, alloy, metal oxides, metal chalcogenides, metal carbides, metal nitrides, nonprecious metal-based N-doped carbon (M-N-C), and heteroatom-doped carbons have been investigated as advanced electrocatalytic materials for HER, OER, and ORR[11,23–30] Among them, carbon-coupled Fe_3C materials with the optimizing morphologies including core–shell structures, nanofibers, nanospheres and nanoribbons were demonstrated to be higher active for ORR, even in acidic solution.[31–40] Nevertheless, transition metal sulfides such as CoS_x[41–46] and NiS_x[47–50] exhibited more efficient catalytic performance for HER and OER. It should be a promising pathway to create the enhancing multifunctional electrocatalytic materials for these electrode reactions by coupling different functionality of several metal compounds in one composite material.[51–53] However, it does not mean that high-efficiency multifunctional eletrocatalysts could be obtained by simply mixing different components on carbon supports. Hence, the challenge in this route is how to realize the synergistically enhancing of several catalytic activities by controlling the formation and homogeneous distribution of different components in carbons and synchronously optimizing the local structures of composites including porosity and conductivity.

Dr. F. T. Kong, X. H. Fan, Prof. A. G. Kong, Z. Q. Zhou,
X. Y. Zhang, Prof. Y. K. Shan
School of Chemistry and Molecular Engineering
East China Normal University
Shanghai 200241, P. R. China
E-mail: agkong@chem.ecnu.edu.cn; ykshan@chem.ecnu.edu.cn

The ORCID identification number(s) for the author(s) of this article can be found under https://doi.org/10.1002/adfm.201803973.

DOI: 10.1002/adfm.201803973

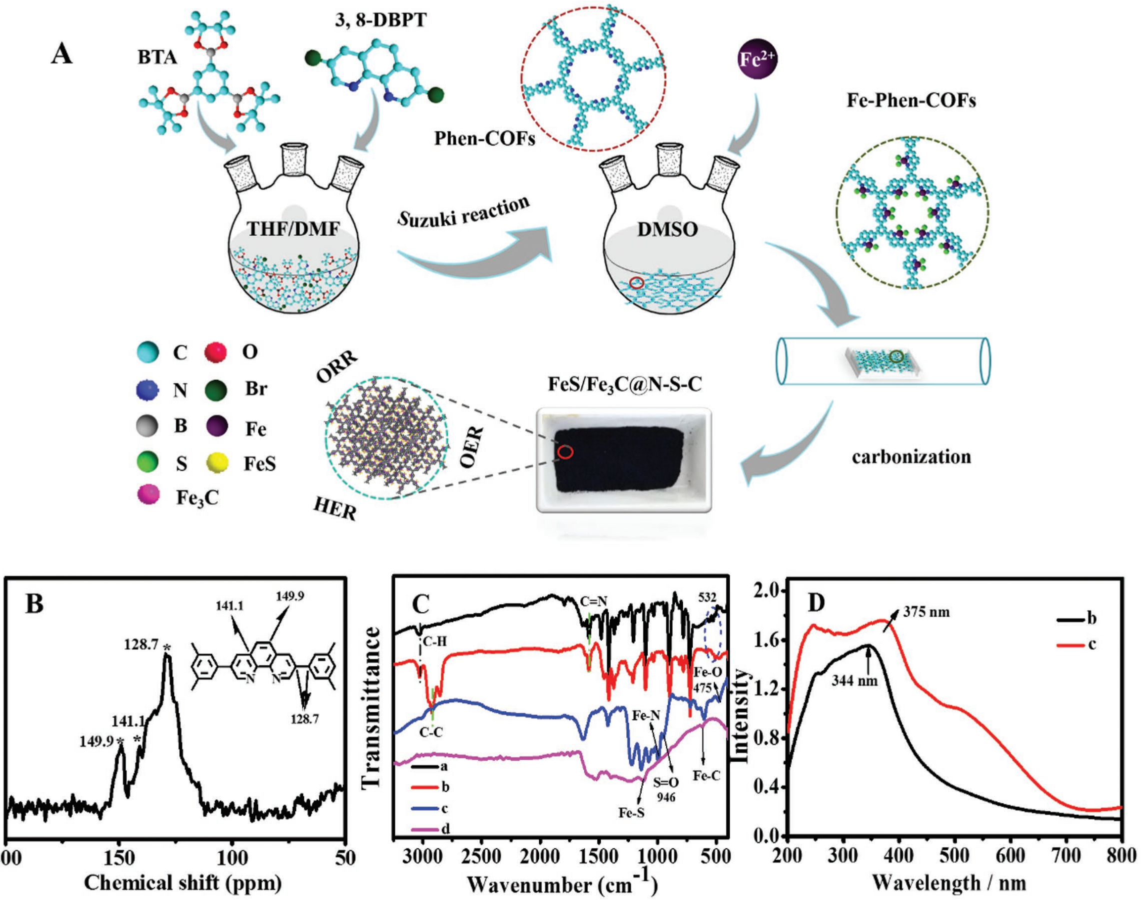

Figure 1. Preparation schematic and structural confirmation of Phen-COFs and Fe-Phen-COFs. A) Schematic representation for the synthesis of Fe-Phen-COFs and the derived FeS/Fe_3C@N-S-C electrocatalysts. B) ^{13}C CP-MAS solid-state NMR spectrum of Phen-COFs. The inset image is chemical formula of Phen-COFs structural unit. C) FT-IR spectra of a) 3, 8-DBPT, b) Phen-COFs, c) Fe-Phen-COFs and d) FeS/Fe_3C@N-S-C-800. D) The UV–vis diffuse reflectance spectra of b) Phen-COFs and c) Fe-Phen-COFs.

Covalent organic frameworks (COFs) with adjustable microcosmic structure and ordered porosity in molecule level can endow the derived carbon materials with target high-efficiency electrocatalytic performance.[54–57] The pyrolysis of COFs could serve as an effective method in precisely controlling the type and distribution of dopants or composites on porous carbons.[58] The thermal conversion of COFs with incorporated porphyrin macrocycles produced more efficient metal-contained ORR electrocatalysts with high-turnover metal-N_4 sites.[59] However, COFs-derived metal-based carbon nanocomposites with high-efficient activities for three reactions are still scarce. Herein, we used 3, 8-dibromophenanthroline (3, 8-DBPL) and 1, 3, 5-benzenetriboronic acid pinacol ester (BTA) as building blocks to synthesize porous COFs with open metal-chelating sites. Fe and the solvent molecules (DMSO) can easily absorbed into such COFs to create Fe—N—C and Fe—O=S moieties as the precursors of Fe_3C and FeS, which were converted into FeS@Fe_3C nanoparticles composite embedding in N-S-codoped carbons (FeS/Fe_3C@N-S-C) by heat treatment. The prepared FeS/Fe_3C@N-S-C composites exhibit high-efficient trifunctional electrocatalytic performance for HER, ORR, and OER in the wide pH range.

2. Results and Discussion

2.1. Confirmation of Phen-COFs and Fe-Phen-COFs

The new Phen-COF structure was synthesized by Suzuki coupling reaction using 3, 8-DBPL and BTA as the rigid building block (**Figure 1**A). The chemical structure of Phen-COFs was confirmed by the solid state ^{13}C cross-polarization magic angle spinning (CP-MAS) NMR spectrum (Figure 1B). The resonance signal near 128.7 ppm was caused by the coupling benzene rings, indicating that the 3, 8-DBPL blocks were successfully coupled to BTA by polymerization. In addition, the peaks at 141.1 and 149.9 ppm were attributed to the carbon atoms in the pyridine ring, confirming the presence of the phenanthroline structure in the prepared Phen-COFs.[60,61] Furthermore, the Fourier transform Infrared (FT-IR) spectra (Figure 1C) of Phen-COFs was similar to that of 3, 8-DBPL, but the C—Br stretching vibrational absorption peak at 532 cm^{-1} of 3, 8-DBPL molecule disappeared after the formation of polymer Phen-COFs, indicating that the C—Br bond broken and coupling polymerization occurred.[57]

The synthesized Fe-Phen-COF networks were obtained from the reflux coordination of Phen-COFs and $Fe(Ac)_2$ in

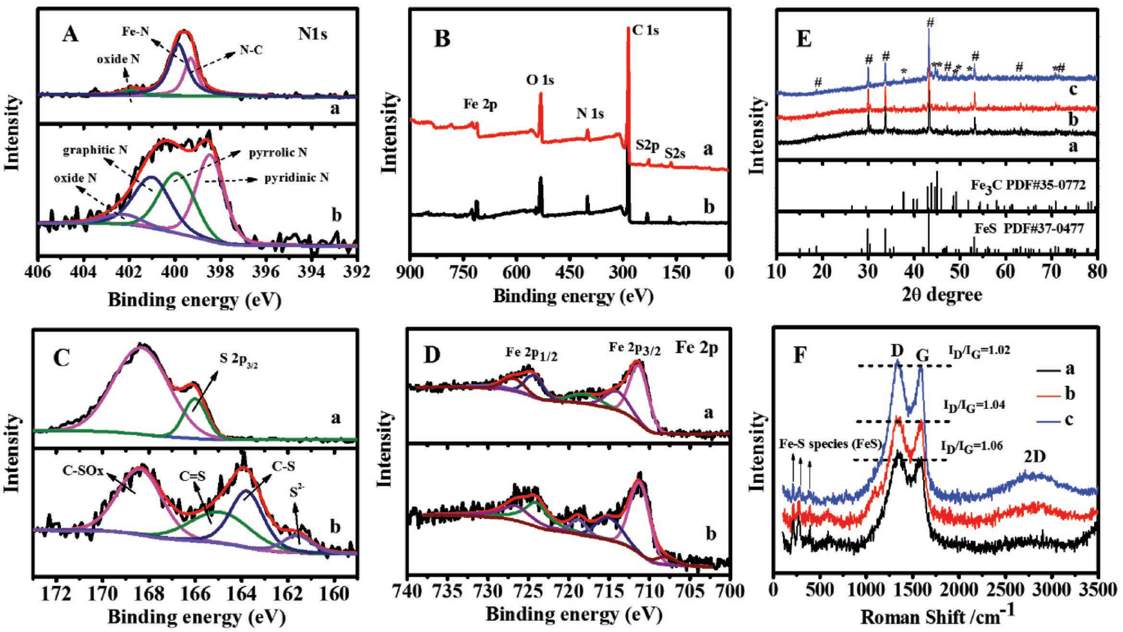

Figure 2. A) The high-resolution N 1s XPS spectrum, B) survey XPS spectra, C) The deconvoluted S 2p XPS spectrum, and D) Fe 2p XPS spectra of a) Fe-Phen-COFs and b) FeS/Fe_3C@N-S-C-800. E) XRD patterns and F) Raman spectra of a) FeS/Fe_3C@N-S-C-700, b) FeS/Fe_3C@N-S-C-800, c) FeS/Fe_3C@N-S-C-900.

DMSO by solvothermal reaction. The IR absorption band at 3030 cm^{-1} (C—H), 1585 cm^{-1} (C=N), and 725 cm^{-1} (ring deformation) of pyridinic rings with similar structures of Phen-COFs disappeared in the Fe-Phen-COFs.[62] The infrared characteristic peak of Fe—N was newly observed at 995 cm^{-1}. The solid-state UV–visible diffuse reflectance spectra (Figure 1D) of Fe-Phen-COFs showed the absorption peak (375 nm), which was from redshift of absorption signals of Phen-COFs (344 nm). It suggested that N-coordinated Fe(II) ions affected the conjugated system of phenanthroline structure.[63] The high-resolution N 1s XPS spectrum (**Figure 2**A-a) of Fe-Phen-COFs revealed the N1s peak around 399.8 eV, which could be attributed to Fe—N moieties.[64] These results testified that Fe(II) ions were coordinated to N-chelate sites in Phen-COFs.

Interestingly, the IR spectra of Fe-Phen-COFs revealed the IR adsorption peak at 946 cm^{-1} and 475 cm^{-1}, corresponding to of S=O and Fe—O that should origin from the direct coordination of DMSO solvent molecules to Fe (II) ions.[62] The XPS survey spectra of Fe-Phen-COFs (Figure 2B-a) indicated the presence of C, N, O, S, Fe elements in Fe-Phen-COFs. The deconvoluted S 2p spectrum of Fe-Phen-COFs (Figure 2C-a) displayed a peak at 166.0 eV, ascribing to the S 2p3/2 signals of coordination species formed by iron ions and DMSO.[65] This further indicated that the coordination complexes of DMSO and iron (II) ions have been involved into Phen-COFs, probably in the form of octahedral $[Fe(Phen)(C_2H_6SO)]^{2+}$ or $[Fe(C_2H_6SO)_6]^{2+}$. The observation of TEM images for Fe-Phen-COFs revealed an amorphous accumulation of compounds (Figure S1, Supporting Information). The coordination compounds will be used to act as the source for generating FeS and Fe_3C nanoparticles and carbon-based matrix in the catalysts.

2.2. Preparation, Composition, and Morphology of FeS/Fe_3C@N-S-C Materials

Owing to the fact that developing the efficient and stable NPMCs for ORR, OER, and HER is of great interest in the commercialization of the high-performance sustainable energy devices on a mass scale, a large variety of the synthesis methods were reported. In general, the different catalysts were prepared by the different methods due to the high dependence of the morphology of the catalysts on the preparation conditions and the difference between the chemical properties of different component elements. However, the normal pyrolysis of simple macrocycles or mixtures of nitrogen and metal precursors only leads to uncontrolled agglomeration or inhomogeneous microstructure and thus insufficient exposure of the active sites and poor mass transport.[66,67] In addition, MOFs are optimal precursors that contain carbon and metal and/or nitrogen precursors together into one framework for the preparation of the nonprecious metal electrocatalysts. Nevertheless, directly carbonized MOFs often lead to metal aggregation and structure breakdown, thus reducing the pore size and surface area. Compared with the traditional synthesis of the nonprecious metal electrocatalysts, the catalyst prepared by us possesses three distinctive features. First, the prepared neo-precursor with Fe-Phen and -DMSO co-chelating sites simultaneously contain carbon, nitrogen, iron, and sulfur sources. In the pyrolysis process, unstable Fe—N and Fe—O=S moieties undergo local decomposition to form small-sized nanoclusters consisting of crystalline iron carbides and iron sulfides and phenanthroline moiety was carbonized to form the N-doped carbon as matrixes of the catalysts. The precursors of the three key component were included in one framework (or one molecule), which display an obvious difference from the synthesis of FeS/Fe_3C

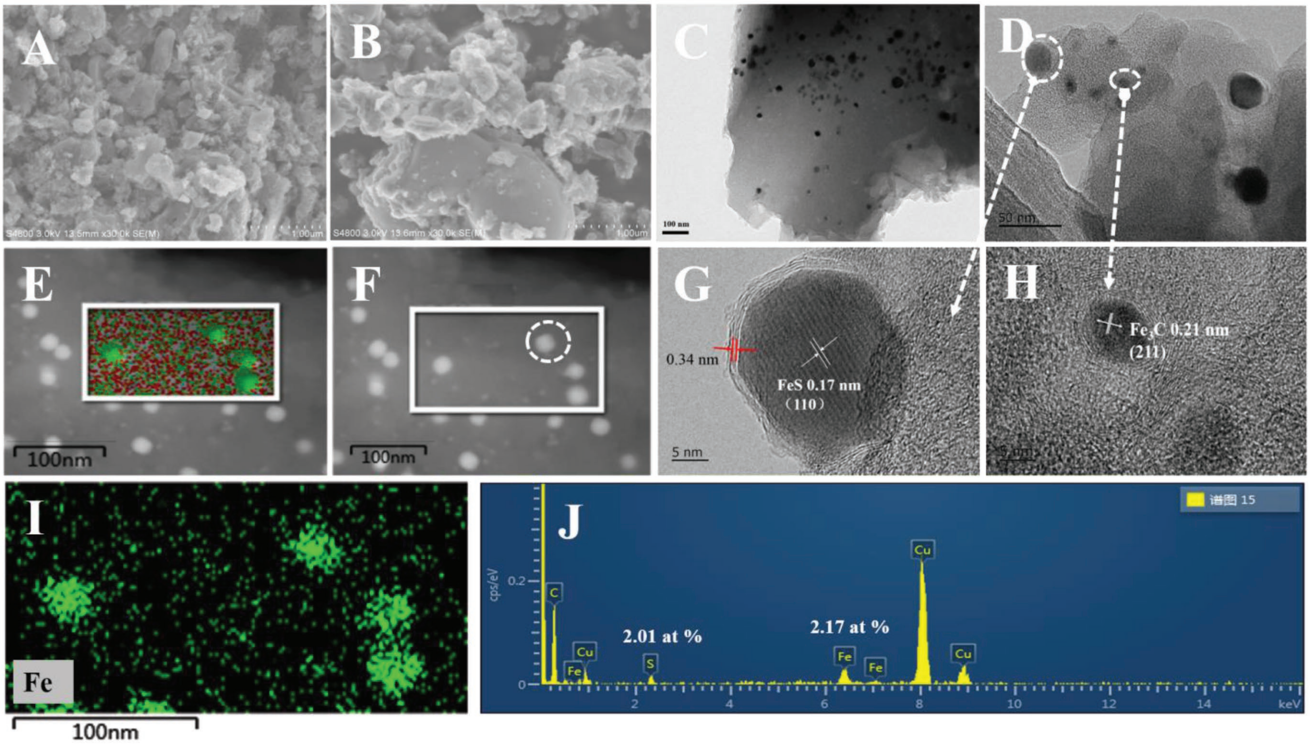

Figure 3. Morphology and structural characterization of as-prepared FeS/Fe$_3$C@N-S-Cs. A,B) SEM (scale bar: 1.00 um) and C,D) TEM images (scale bar: 100 and 50 nm) of FeS/Fe$_3$C@N-S-C-800. G,H) HRTEM images (scale bar: 5 nm) of FeS/Fe$_3$C@N-S-C-800,revealing lattice fringes of the FeS, Fe$_3$C phase, and wrapped graphitic carbon edges, respectively. E,F) HAADF-STEM image and I) elemental mappings for Fe of FeS/Fe$_3$C@N-S-C-800. J) STEM-EDX images of FeS at the white circle mark in H of FeS/Fe$_3$C@N-S-C-800.

loaded on the nonmetal doped carbons reported in the literature.[68] Next, the unstable Fe—N and Fe—O=S moieties were included in one framework as precursor, which is in favor of creating the higher active site density and the uniform distribution of the active species. Finally, the Fe—N moiety closely neighbor Fe—O=S moiety in one framework as precursor, which facilitates the construction of the two-phase composite structures consisting of the iron carbides and iron sulfides in the nanoparticles (Figure S2, Supporting Information). Such structures are conducive to the synergistic interaction of Fe$_3$C and FeS.

The large-angle X-ray diffraction patterns (XRDs) of FeS/Fe$_3$C@N-S-C carbonized at different temperatures were shown in Figure 2E. The diffraction humps at $2\theta = 18.7°$ (101), 29.9° (110), 33.6° (112), 47.1° (211), 53.1° (300), 63.2° (008), and 71.4° (118) were assigned to hexagonal FeS crystal phase (PDF#37-0477). The rest diffraction peaks at $2\theta = 37.7°$ (210), 44.6° (220), and 45.8° (112) agreed well with the characteristic diffraction peaks of orthorhombic Fe$_3$C crystal phase (PDF#35-0772). These results indicated that FeS and Fe$_3$C phases were formed after pyrolysis treatment of Fe-Phen-COFs. There were no obvious detectable diffraction signals originating from the (002) and (101) planes of graphitic carbons,[69] which may be due to higher diffraction intensity of Fe$_3$C and FeS nanoparticles. However, the Raman spectroscopy (Figure 2F) of FeS/Fe$_3$C@N-S-C obtained at different pyrolysis temperatures showed the clear C—C adsorption signals at 1338 and 1588 cm^{-1}, assigning to typical D and G bands of carbon materials. The relative strength of these two bands (I_D/I_G) often evaluated the content of defects and average crystallite size of the sp^2 domains in the derived FeS/Fe$_3$C@N-S-C samples.[70–72] The calculated I_D/I_G values were 1.06, 1.04, and 1.02 for the FeS/Fe$_3$C@N-S-C-700, -800, and -900, respectively. It suggested that the crystallite domains of carbon layers gradually increased with the elevation of carbonization temperature.

The FeS/Fe$_3$C@N-S-C-800 observed in scanning electron microscope (SEM) image (**Figure 3**A,B) showed a piece-stacked particle morphology. A clearer transmission electron microscopy (TEM) image (Figure 3C,D) of FeS/Fe$_3$C@N-S-C-800 exhibited that some core–shell structures were embedded in the carbon matrix. The core particles had two different crystalline phases. The observation of high-resolution transmission electron microscopy (HRTEM) (Figure 3G,H) further displayed that these core particles with small size in diameter were encapsulated into the graphitic carbon layer. The lattice spacing with a *d*-spacing of 2.11 and 1.72 Å agreed well with the distance of (211) and (110) planes of Fe$_3$C and FeS, respectively.[62] The two-phase composite structures consisting of iron carbides and iron sulfides in the nanoparticles were clearly observed on the surface of carbon layers (Figure S2, Supporting Information). Furthermore, high-angle annular dark field scanning transmission electron microscopy (HAADF-STEM) and elemental mappings images (Figure 3E,F,I) were used to verify Fe elemental distribution in the FeS/Fe$_3$C@N-S-C-800. The analysis of HRTEM combined with STEM-EDX (Figure 3J) indicated that the presence of FeS in FeS/Fe$_3$C@N-S-C-800 with the atomic

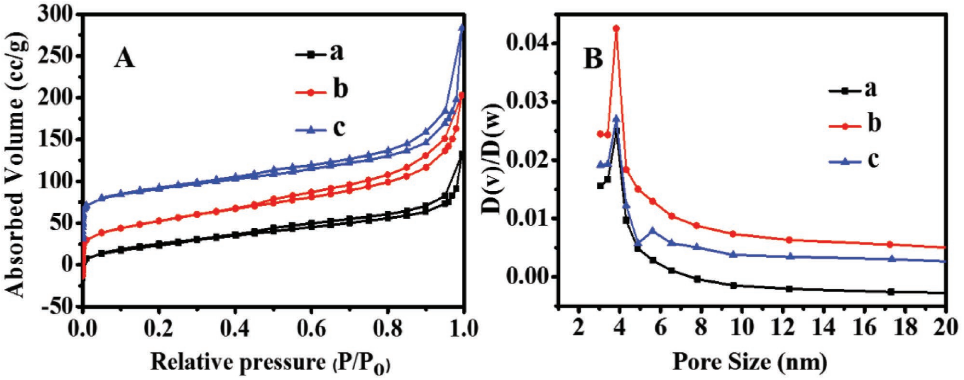

Figure 4. A) N_2 adsorption–desorption isotherms. B) Pore distribution curves obtained by BJH method based on the adsorption branch. a) FeS/Fe_3C@N-S-C-700, b) FeS/Fe_3C@N-S-C-800, and FeS/Fe_3C@N-S-C-900.

percentage ratio of Fe (2.17 at%) and S (2.01 at%) was approximately similar to 1:1 in the crystalline particles. The coexistence of Fe_3C@C and FeS@C core–shell structures in derived carbons avoided the serious agglomeration of Fe_3C and FeS nanoparticles and provided a stable carbon peripheral protection for them.[25,73] Core–shell Fe_3C@C and FeS@C may synergistically exert stable multifunctional electrocatalytic activity toward ORR, HER, and OER.

The nitrogen adsorption–desorption analysis indicates that the as-synthesized FeS/Fe_3C@N-S-C materials possessed the typical type I isotherms (**Figure 4**A). Specifically, the adsorption of N_2 increased sharply at a lower relative pressure P/P_0, indicating the presence of micropores in the FeS/Fe_3C@N-S-Cs.[74] A remarkable increase in the middle and high P/P_0 with a clear hysteresis loop also confirmed the presence of mesopores and some macropores. The listed parameters in **Table 1** showed that FeS/Fe_3C@N-S-C-800 possessed the highest Bruauer–Emmett–Teller specific surface area (S_{BET}) of 288 $m^2\ g^{-1}$ and total pore volume of 0.35 $cm^3\ g^{-1}$. This S_{BET} is not very higher than other carbon-based materials, probably owing to higher mass content of Fe_3C and FeS particles. The micropore and mesoporous pore size obtained from calculation by Horvaih–Kawazoe (HK) (Figure S3, Supporting Information) and Barrett–Joyner–Halenda (BJH) (Figure 4B) method was centered at 0.49 and 3.8 nm. These N_2-sorption behaviors testified the hierarchical porosities of FeS/Fe_3C@N-S-Cs, which could facilitate the exposure of more active species and enhance the mass-transport capacity in the catalysts.

2.3. Surface Ingredients on FeS/Fe_3C@N-S-Cs

The SEM elemental mapping results of FeS/Fe_3C@N-S-C-800 (Figure S4, Supporting Information) showed that a reasonable distribution of Fe, S, C, and O atoms in the surface of the prepared catalyst. XPS measurements were further conducted to investigate the chemical composition and the chemical environment of component elements of FeS/Fe_3C@N-S-C-800. The survey XPS spectrum of FeS/Fe_3C@N-S-C-800 (Figure 2B-b) also revealed the presence of C, N, O, S, and Fe elements, which indicated that the N, Fe, and S elements were successfully implanted in the carbon frameworks. The surface N content of FeS/Fe_3C@N-S-C-800 is about 3.55 at%, lower than that of Fe-Phen-COFs precursors (4.54 at%, **Table 2**). The high-resolution N 1 s spectra (Figure 2A-b) of FeS/Fe_3C@N-S-C-800 were deconvoluted into four peaks centered at 398.4, 400.0, 401.1, and 402.3 eV, corresponding with pyridinic-N, pyrrolic-N, graphitic-N, and oxidized-N, respectively.[75] It is clear that the pyridinic N and graphitic N were dominant N species in the carbon frameworks, which were believed as more effective N-doping type for enhancing activity of carbons.[76] The high-resolution Fe 2p survey spectra (Figure 2D-b) of FeS/Fe_3C@N-S-C-800 revealed photoelectron signals in the Fe $2p_{1/2}$ and Fe $2p_{3/2}$ region, confirming the presence of Fe (II) and/or Fe (III) state.[77,78] Furthermore, the peak at a binding energy of 707.8 eV in Fe $2p_{3/2}$ region also revealed the presence of Fe_3C.[79] For the S 2p spectrum in Figure 2C, four well-defined peaks were observed. Two peaks located at 163.7 and 164.9 eV were attributed to the existence of thiophene-like (−C−S−, −C=S−), while the peak at 168.4 eV was characteristic of the oxide of sulfur ($-SO_x$). The two peaks confirmed that S species have also been doped in the carbon lattices or edges in the form of C−S, C=S or C−SO_x.[80,81] The S 2p peak at 161 eV was assigned to S^{2-} structure.[82] It proved that S ions from the decomposition of Fe-DMSO coordination compounds reacted with Fe(II) and formed FeS nanoparticles encased in carbon layers. Fe−S species in the FeS/Fe_3C@N-S-Cs were also found by several peaks below 500 cm^{-1} in Raman spectra,[83] agreeing with FT-IR and XRD results.

Table 1. The textural parameters of FeS/Fe_3C@N-S-C-*n* materials.

Samples	S_{BET} [$m^2\ g^{-1}$]	$S_{\mathrm{micropore}}$ [$m^2\ g^{-1}$]	S_{exteral} [$m^2\ g^{-1}$]	V_{total} [cc g^{-1}]	$V_{\mathrm{micropore}}$ [cc g^{-1}]	d_{HK} [nm]	d_{BJH} [nm]
FeS/Fe_3C@N-S-C-700	166	118	48	0.24	0.07	0.49	3.8
FeS/Fe_3C@N-S-C-800	288	200	88	0.35	0.11	0.49	3.8
FeS/Fe_3C@N-S-C-900	266	158	108	0.41	0.07	0.49	3.8

Table 2. The surface species analyses of Fe-Phen-COFs and FeS/Fe_3C@N-S-C-800 by XPS (at%).

Samples	N	N_{Pyd}	N_{Pyr}	N_g/N-C	Fe-N	N-oxide
Fe-PTCPs	4.54	—	—	32.4	61.7	5.9
FeS/Fe_3C@N-S-C-800	3.55	31.6	52.6	10.2	—	5.6

2.4. Local Microstructures of FeS/Fe_3C@N-S-Cs

In order to further understand and explore the catalytic behavior of the prepared catalysts, FeS/Fe_3C@N-S-C catalyst was further characterized with X-ray absorption spectroscopy (XAS) and ^{57}Fe Mössbauer spectroscopy measurements to confirm the chemical environment of the iron atoms in the prepared catalysts. As can be seen in **Figure 5**A, the X-ray absorption near edge structure (XANES) edge of FeS/Fe_3C@N-S-C shifted to higher energy relative to the absorption edge of Fe foil, indicating the increase of the Fe oxidation state. The local structural information of the iron species in the FeS/Fe_3C@N-S-C catalyst was probed using Fourier transformed X-ray absorption fine structure (FT-EXAFS) spectroscopic analysis (R space). The three FT peaks displayed in Figure 5B clearly revealed iron-based local microstructures in the FeS/Fe_3C@N-S-C catalyst.[69] The FT peak at ≈1.99 Å can be well defined as a Fe—S configuration with a bond length of ca. 2.39 Å (all the radial distances given in figure 5B are without phase correction, the true bond length = 1.99 + 0.4 Å because of a phase shift). The FT peak at ≈2.45 Å can be fitted as Fe—Fe scattering with a bond length of ca. 2.85 Å. This bond length belonged to the Fe-Fe pair in iron sulfide.[84] The FT peak at ≈1.51 Å may arise from the Fe—N / Fe—C / Fe—O scattering. However, it should be noted that an inherent limitation of XAS is the inability to differentiate N from C and O due to similar atomic numbers of them. We cannot use FT EXAFS to conclusively identify the presence or absence of iron nitrides or carbides in the final catalyst.[84] Therefore, we measured ex situ ^{57}Fe Mössbauer spectroscopy to identify the different chemical environment of iron in FeS/Fe_3C@N-S-C sample. The results were shown in Figure 5C. The spectrum was composed of four components: three sextets and one singlet. The fitted Mössbauer parameters were shown in **Table 3**. The singlet was assigned to γ-Fe, while the hyperfine parameters of the three sextets S1 (sextet 1), S2, S3 corresponded to iron sulfide (FeS), iron carbide (Fe_3C), and α-Fe, respectively.[85] The results of the FT EXAFS and ^{57}Fe Mössbauer spectroscopy analysis clearly certified that the prepared FeS/Fe_3C@N-S-C catalysts contain FeS and Fe_3C as the main components.

2.5. Electrochemistry Properties for the ORR

The electrocatalytic properties of FeS/Fe_3C@N-S-C toward ORR were first investigated in alkaline medium by cyclic voltammetry (CV) and rotating disc electrode (RDE) techniques. An impressive peak potential of FeS/Fe_3C@N-S-C-800 was found to emerged at 0.85 V (vs RHE) in O_2-saturated 0.1 M KOH solution, in contrast to the nonfeature CV curves in N_2-saturated solution (**Figure 6**A), suggesting that the FeS/Fe_3C@N-S-C catalyst possessed high efficiency electrocatalytic activity for ORR in alkaline medium. Additionally, to further explore the ORR properties of the prepared catalytic materials, the polarization curves for FeS/Fe_3C@N-S-C-*n* prepared at different pyrolysis temperatures were obtained at a scan rate of 5 mV s^{-1} and a rotation rate of 1600 rpm (Figure 6B), displaying that FeS/Fe_3C@N-S-C-800 possessed the best ORR activity in 0.1 M KOH solution. The half-wave potential on FeS/Fe_3C@N-S-C-800 ($E_{1/2}$ = 0.87 V) was more positive than that on the commercial Pt/C (0.84 V). The corresponding current density (5.2 mA cm^{-2} at 0.2 V) was comparative to that on the Pt/C-JM catalyst (20 wt%, Johnson Matthey). The Tafel slope of ORR on FeS/Fe_3C@N-S-C-800 (90 mV $decade^{-1}$) (Figure S5A, Supporting Information) was smaller than those on other catalysts, signifying the favorable ORR kinetics of FeS/Fe_3C@N-S-C-800 in 0.1 M KOH medium.

The ORR catalytic behaviors of FeS/Fe_3C@N-S-C-*n* were also evaluated in 0.1 M $HClO_4$ electrolyte. The corresponding CV curves (Figure 6D) confirmed that FeS/Fe_3C@N-S-C-800 had an obvious cathodic peak potential (E_p = 0.71 V) in O_2-saturated 0.1 M $HClO_4$ solution. The RDE polarization curves of FeS/Fe_3C@N-S-C-800 (Figure 6E) showed that the half-wave potential was about 160 mV negative shift compare with a commercial Pt/C catalyst (0.80 V), indicating the better ORR catalytic performance compared with the reported non-precious catalysts in acidic electrolyte. The diffusion-limiting current of ORR on FeS/Fe_3C@N-S-C-800 was 5.1 mA cm^{-2} at 0.2 V, which was slightly lower than that over the commercial Pt/C catalyst (5.3 mA cm^{-2} at 0.2 V). Compared with other

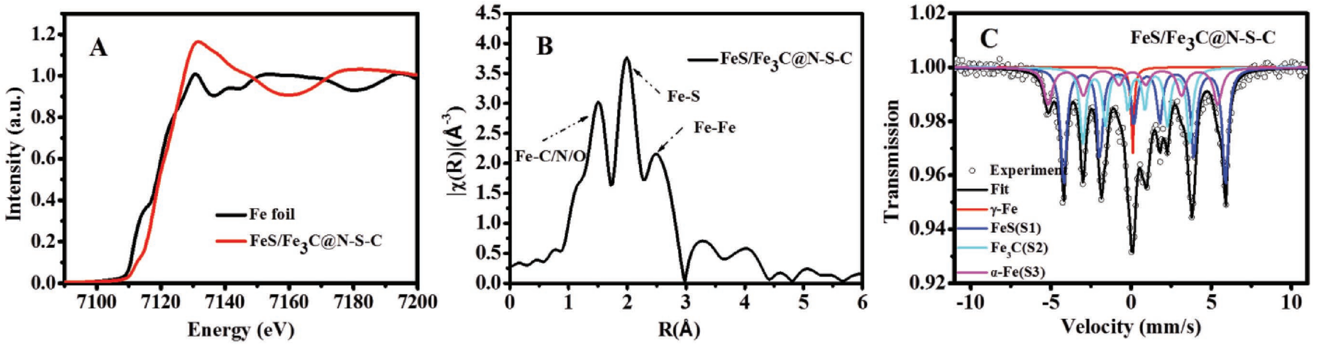

Figure 5. A) Fe K-edge XANES spectra of FeS/Fe_3C@N-S-C-800 and Fe foil. B) Fourier transform EXAFS of FeS/Fe_3C@N-S-C-800. C) ^{57}Fe Mössbauer spectrum of the FeS/Fe_3C@N-S-C-800 catalyst.

Table 3. The fitted Mössbauer parameters for the FeS/Fe$_3$C@N-S-C-800 catalyst at room temperature.

Samples		IS [mm s^{-1}]	QS [mm s^{-1}]	HF [Tasel]	LW [mm s^{-1}]	Assignment
FeS/Fe$_3$C @N-S-C	Singlet	0.08	—	—	0.28	γ-Fe
	Sextet 1	0.91	0.15	31.35	0.46	FeS
	Sextet 2	0.33	0.00	20. 70	0.44	Fe$_3$C
	Sextet 3	0.10	–0.03	32.84	0.64	α-Fe

catalytic materials, the smaller Tafel slope on FeS/Fe$_3$C@N-S-C-800 (150 mV decade^{-1}) (Figure S5B, Supporting Information) revealed a favorable reaction kinetics in 0.1 M HClO$_4$ solution. These results imply that FeS/Fe$_3$C@N-S-C-800 has the highly efficient ORR catalytic activity in both alkaline and acidic media.

The ORR electrocatalytic activities of the prepared FeS/Fe$_3$C@N-S-C-*n* were also investigated in neutral 0.01 M PBS buffer. As shown in Figure 6G, a well-defined cathodic peak appeared at 0.65 V (vs RHE) in O$_2$-saturated 0.01 M PBS electrolyte and featureless cyclic voltammogram existed in N$_2$-saturated buffer, which indicated that the FeS/Fe$_3$C@N-S-C-*n* catalysts have the ORR activity in neutral electrolyte. It can be seen in Figure 6H that the LSV curves of the as-prepared N-S-C-800, FeS/Fe$_3$C@N-S-C-*n*, and Pt/C catalysts were obtained at a rotating speed of 1600 rpm. Remarkably, the FeS/Fe$_3$C@N-S-C-800 catalyst exhibited a half-potential ($E_{1/2}$ = 0.56 V) comparable to that on the Pt/C catalyst (0.575 V) for ORR and higher limiting current (5.5 mA cm^{-2} at –0.1 V) than that over the Pt/C catalyst (5.3 mA cm^{-2} at –0.1 V) in the neutral electrolyte. To gain insight into the ORR activity, Tafel plots (Figure S5C, Supporting Information) on the as-prepared catalysts were further studied. The results indicate that Tafel slope value of 85 mV dec^{-1} for the FeS/Fe$_3$C@N-S-C-800 is much lower than that for all the samples tested. The relatively lower Tafel slope indicated that FeS/Fe$_3$C@N-S-C-800 has an outstanding ORR reaction kinetics.

The electrocatalytic durability of FeS/Fe$_3$C@N-S-C-800 was investigated by chronoamperometric method in three electrolytes. As displayed in the Figure 6C,F,I, no obvious change in the peak potential of the CV curves was observed before and after running 5000 cycles in O$_2$-saturated 0.1 M KOH, 0.1 M HClO$_4$ as well as 0.01 M PBS solutions, indicating high survivability of the catalytic activity structures. These results suggested

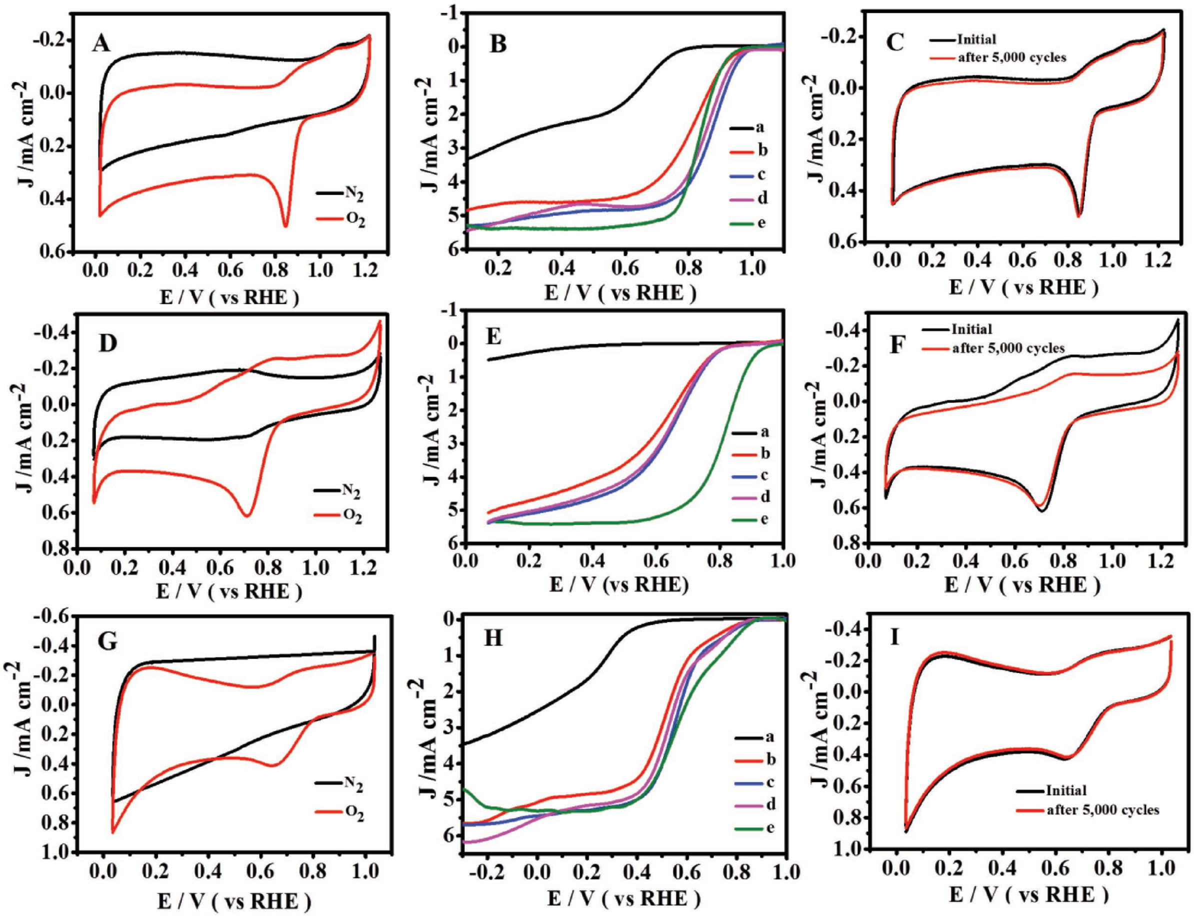

Figure 6. Cyclic voltammograms (CV) obtained in O$_2$ and N$_2$ saturated A) 0.1 M KOH, D) 0.1 M HClO$_4$, and G) 0.01 M PBS electrolytes of FeS/Fe$_3$C@N-S-C-800. Polarization curves of a) N-S-C-800, b) FeS/Fe$_3$C@N-S-C-700, c) FeS/Fe$_3$C@N-S-C-800, d) FeS/Fe$_3$C@N-S-C-900, and e) commercial Pt/C (20 wt%) in O$_2$ saturated B) 0.1 M KOH, E) 0.1 M HClO$_4$, and H) 0.01 M PBS electrolytes. CVs run for 5000 cycles recorded in O$_2$ saturated in C) 0.1 M KOH, F) 0.1 M HClO$_4$, and I) 0.01 M PBS electrolytes for FeS/Fe$_3$C@N-S-C-800 (electrode rotation speed, 1600 rpm; scan rate, 5 mV s^{-1}).

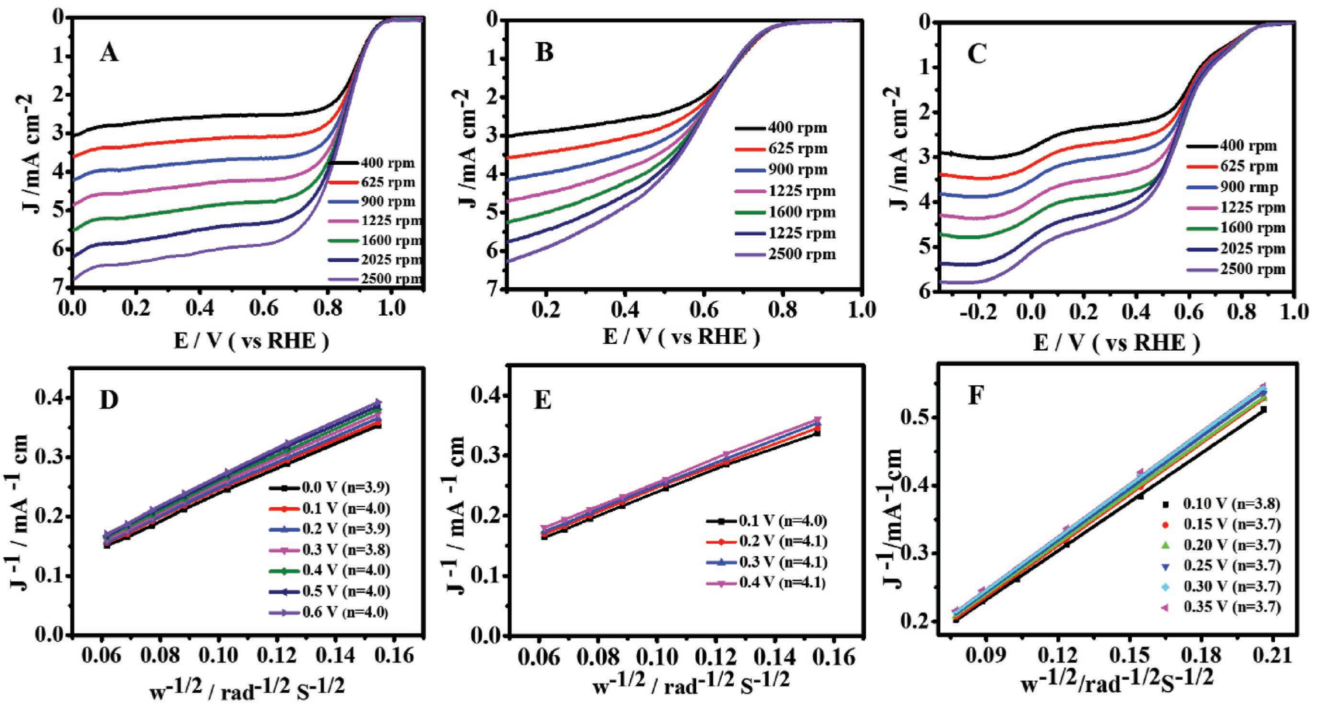

Figure 7. LSV curves of FeS/Fe$_3$C@N-S-C-800 at different rotation rates in A) 0.1 M KOH, C) 0.1 M HClO$_4$, and E) 0.01 M PBS electrolytes. K-L plot and the corresponding electron transfer numbers for FeS/Fe$_3$C@N-S-C-800 in B) 0.1 M KOH, D) 0.1 M HClO$_4$, and F) 0.01 M PBS electrolytes.

that the FeS/Fe$_3$C@N-S-C-800 had better ORR stability and durability than commercial Pt/C in a wide pH range. The N-S-codoping carbon-encapsulated FeS@Fe$_3$C nanostructures might restrain the dissolution and agglomeration of Fe$_3$C and FeS nanoparticles, thus enhancing the electrocatalytic stability and durability.

The ORR kinetics process of the FeS/Fe$_3$C@N-S-C-800 catalysts was investigated according to the RDE polarization curves at different rotating rates in three media (**Figure 7**A–C). The corresponding K-L plots (Figure 7D–F) obtained from the polarization curves for FeS/Fe$_3$C@N-S-C-800 between 0 and 0.6 V in 0.1 M KOH, 0.1 to 0.4 V in 0.1 M HClO$_4$ and 0.1 V to 0.35 V in 0.01 M PBS electrolytes exhibit the parallel lines at various potentials, indicating a first-order process with the same number of electrons transferred per O$_2$ molecule in the oxygen electroreduction at different potentials.[86] The transferred electron numbers (n) derived from the slopes of the linear K-L plots at 0.3 V (vs RHE) on FeS/Fe$_3$C@N-S-C-800 in alkaline, neutral, acidic solutions were 3.9, 3.7 and 4.1 respectively, confirming that ORR catalyzed by FeS/Fe$_3$C@N-S-C-800 occurs mainly by the direct 4-electron reduction pathway from O$_2$ to H$_2$O within a wide pH range with low overpotential.

2.6. Electrochemistry Properties for the OER and HER

To evaluate the electrocatalytic activity for OER, the OER LSV curves on FeS/Fe$_3$C@N-S-C-*n* materials were measured in O$_2$-saturated 1 M KOH, 0.01M PBS and 0.5 M H$_2$SO$_4$ solutions, respectively. Although the OER activity of FeS/Fe$_3$C@N-S-C-800 was not prominent under acidic (2.41 V for 10 mA cm^{-2}, Figure S6A, Supporting Information) and neutral conditions (2.32 V for 10 mA cm^{-2}, Figure S7A, Supporting Information), impressively, FeS/Fe$_3$C@N-S-C-800 afforded a current density of 10 mA cm^{-2} at an electrode potential of 1.80 V under alkaline conditions (**Figure 8**A). This fact illustrates that the OER catalytic activity of FeS/Fe$_3$C@N-S-C-800 is comparable to those of the analogous catalysts by recently reported (see Table S1 in the Supporting Information for detailed comparison). However, there are still some gaps compared with the state-of-the-art IrO$_2$ catalyst. From Tafel plots constructed by the polarization curves (LSV curves in Figure 8A), the Tafel slopes can be obtained by fitting of the straight line segment of Tafel plots[87] as shown in Figure 8B, which shows a Tafel slope of 81 mV dec^{-1}, implying a relatively fast kinetic reaction rate on FeS/Fe$_3$C@N-S-C-800 for OER. Such kinetic feature is very similar to those of the reported catalysts.[42,88–90]

The catalytic performance of FeS/Fe$_3$C@N-S-C-800 for HER was also explored in N$_2$-saturated 0.5 M H$_2$SO$_4$, 0.01 M PBS and 1 M KOH electrolytes, respectively. The LSV curves in Figure 8C exhibit the high-efficiency catalytic activity of FeS/Fe$_3$C@N-S-C-800 for HER in 0.5 M H$_2$SO$_4$ solution. The overpotential of HER on FeS/Fe$_3$C@N-S-C-800 at a current density of 10 mA cm^{-2} was −174 mV, more positive than that on other FeS/Fe$_3$C@N-S-Cs catalysts. The catalytic activity of FeS/Fe$_3$C@N-S-C-800 for HER was better than those of the reported nonprecious electrocatalysts under acidic conditions in the literature, such as Fe$_3$C/Mo$_2$C@NPGC (−980 mV),[91] Co$_9$S$_8$@C (−240 mV),[92] and Mo$_2$C@NC-2-750 (−240 mV)[93] (more details were listed in Table S2 in the Supporting Information). The FeS/Fe$_3$C@N-S-C electrode exhibited a catalytic activity closer to Pt/C electrode for HER compared with the analogous catalyst.

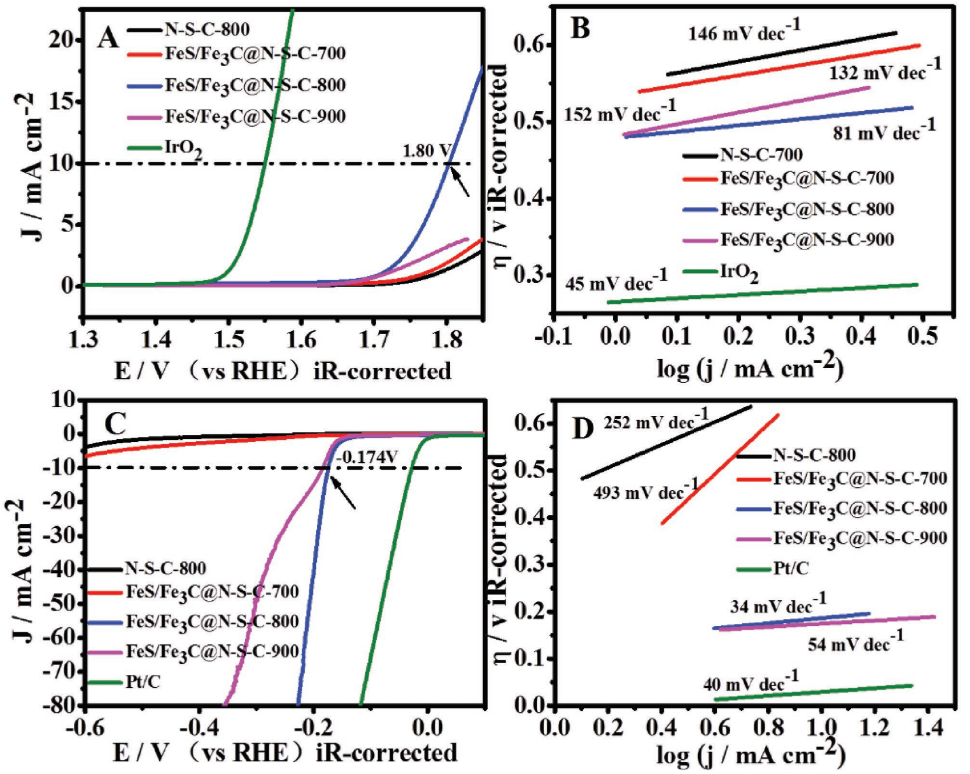

Figure 8. A) The LSV curves and B) corresponding Tafel slopes on different catalysts for OER in 1 M KOH solution. C) The LSV curves and D) corresponding Tafel slopes on different catalysts for HER in 0.5 M H_2SO_4 solution (electrode rotation speed, 1600 rpm; scan rate, 5 mV s^{-1}).

Tafel slope of HER over FeS/Fe_3C@N-S-C-800 (Figure 8D) was 34 mV dec^{-1} and the smallest among the tested materials (493 mV dec^{-1} for FeS/Fe_3C@N-S-C-700, 54 mV dec^{-1} for FeS/Fe_3C@N-S-C-900, and 40 mV dec^{-1} for Pt/C), indicating an intrinsically improved HER kinetics. Moreover, FeS/Fe_3C@N-S-C-800 also exhibited proper catalytic performance for HER with the overpotential of −446 mV in 1 M KOH electrolyte and −798 mV at a current density of 10 mA cm^{-2} in 0.01 M PBS buffer (Figures S6C and S7C, Supporting Information). These results attest that FeS/Fe_3C@N-S-C-800 has the effective HER activity in a wide pH range.

Moreover, the variation rule of electrocatalytic activity of FeS/Fe_3C@N-S-C-800 for ORR, OER and HER with the PH of electrolyte (**Table 4**) was consistent with the literature results.[94–96] These results sufficiently illustrated that FeS/Fe_3C@N-S-C-800 catalyst possesses multifunctional electrocatalytic properties in the wide range of PH.

The long-term durability of the FeS/Fe_3C@N-S-C-800 catalyst for OER and HER was investigated by linear sweep voltammetry (LSV) technique. As showed in Figure S8A,D (Supporting Information), the potential of the OER and HER polarization curves at the current density of 10 mA cm^{-2} on the catalysts in 1 M KOH solution slightly shifted (≈20 and ≈15 mV) after running 2000 cycles. In the meantime, by the same durability measurement method, the negligible potential shift of the OER and HER polarization curves was observed at the current density of 10 mA cm^{-2} in 0.5 M H_2SO_4 electrolyte (Figure S8B,E, Supporting Information) and 0.01 M PBS buffer (Figure S8C,F, Supporting Information). These results indicated the slight degradation of FeS/Fe_3C@N-S-C-800 for OER and HER in a wide pH range. The good durability of the FeS/Fe_3C@N-S-C-800 catalyst could be derived from its unique constitution with metal species closely wrapped in the carbon matrix.

For exploring the possibility of FeS/Fe_3C@N-S-C-800 catalyst in the practical application, the home-made zinc–air batteries were assembled using the FeS/Fe_3C@N-S-C-800 catalyst as the active air electrode and Zn foil as the anode for an energy-related practical application (**Figure 9**). We also constructed

Table 4. The comparison of the electrochemical catalytic properties of the FeS/Fe_3C@N-S-C-800 catalyst in the wide range of PH.

Sample	ORR						OER/HER					
	0.1 M KOH		0.1 M $HClO_4$		0.01 M PBS		1 M KOH		0.5 M H_2SO_4		0.01 M PBS	
FeS/Fe_3C@N-S-C-800	E_{onset}	$E_{1/2}$	E_{onset}	$E_{1/2}$	E_{onset}	$E_{1/2}$	η_{OER}	η_{HER}	η_{OER}	η_{HER}	η_{OER}	η_{HER}
	1.02	0.87	0.88	0.64	0.92	0.54	0.57	0.45	1.18	0.17	1.09	0.80

Note: E_{onset} and $E_{1/2}$ represent the onset potential (V vs RHE) and half-wave potential (V vs RHE) of ORR, respectively. η_{OER}/η_{HER} represent the overpotential (V vsRHE) at the current density of 10 mA cm^{-2} of OER or HER.

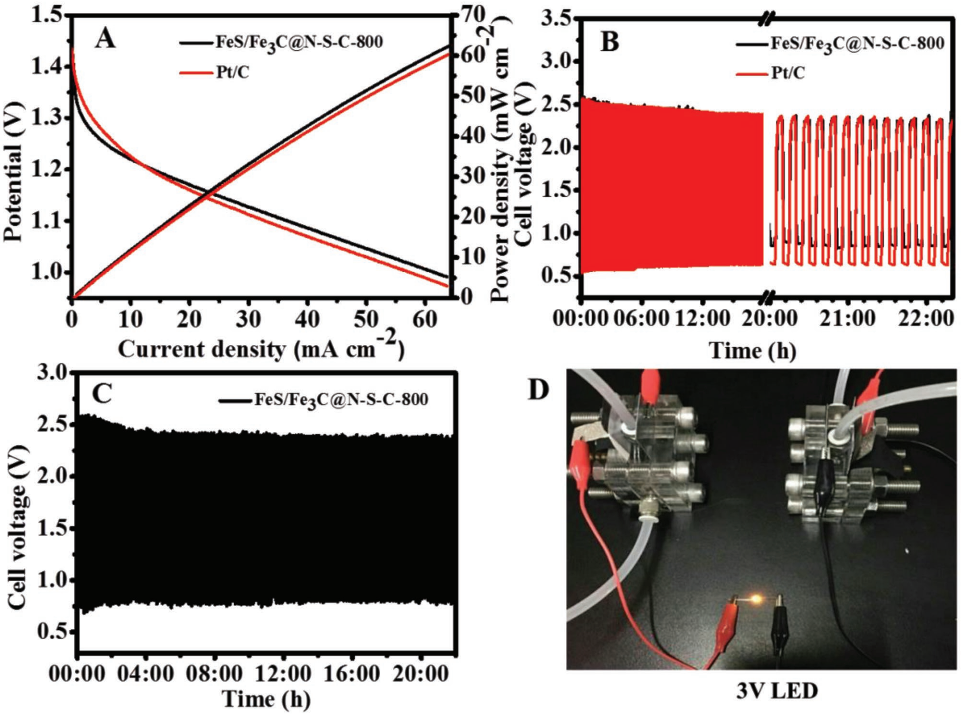

Figure 9. The FeS/Fe_3C@N-S-C-800-based zinc–air batteries. A) Polarization and power density curves of the zinc–air batteries with the FeS/Fe_3C@N-S-C-800 or Pt/C as catalysts. B) Galvanostatic discharge–charge cycling curve at 20 mA cm^{-2} of rechargeable zinc–air battery with different catalysts. C) Galvanostatic discharge–charge cycling curves at 20 mA cm^{-2} of rechargeable zinc–air batteries with the FeS/Fe_3C@N-S-C-800 catalyst. D) Photograph of a light-emitting diode (LED, 3 V) powered by two batteries connected in series.

reference battery using Pt/C catalyst loaded on carbon cloth as the air electrode. Figure 9A displayed the polarization and power density curves for the FeS/Fe_3C@N-S-C-800 and Pt/C air electrodes. The measured open-circuit potentials (OCPs) of the resultant zinc–air batteries were as high as 1.43 and 1.44 V for FeS/Fe_3C@N-S-C-800- and Pt/C-derived air electrodes respectively. The FeS/Fe_3C@N-S-C-800 catalyst showed a peak current density of ≈65 mA cm^{-2} and a peak power density of ≈63 mW cm^{-2}, which was higher than that of the Pt/C-based counterpart (peak current density: ≈65 mA cm^{-2}; peak power density: ≈60 mW cm^{-2}). Moreover, durability of the batteries has also been evaluated using a galvanostatic recurrent pulse method at a constant current density of 20 mA cm^{-2} for 24 h with a 5 min to recharge and 5 min to discharge. As shown in Figure 9B, the FeS/Fe_3C@N-S-C-800 catalyst produced an initial charge potential of 2.34 V and discharge potential of 0.85 V with a voltage gap of 1.49 V, confirming a higher round-trip efficiency of 37.6% compared to 27.1% of Pt/C electrode. After 24 h of circulation, the zinc–air battery with the FeS/Fe_3C@N-S-C-800 catalyst showed high stability (Figure 9C), whereas the control zinc–air battery with the Pt/C catalyst suffered a slightly decline in the discharge potential after 24 h. Both results from the galvanodynamic test and galvanostatic discharge–charge test indicated that the electrocatalytic performance and stability of the FeS/Fe_3C@N-S-C-800 catalyst were superior to that of the Pt/C (20 wt%) catalyst in the zinc–air battery test. As an example for practical application (Figure 9D), multiple zinc–air batteries with serial connection were fabricated and integrated into circuits to power a red light-emitting diode (LED, 3 V), which exhibit an excellent operation stability. So we believe that FeS/Fe_3C@N-S-C-800 catalyst is a promising catalyst toward the new renewable energy technologies.

In order to gain insight into the catalytic origin and behavior of FeS/Fe_3C@N-S-C-800 during ORR, OER, and HER, the catalysts without FeS/Fe_3C (N-S-C-800) was prepared (see the Experimental Section) and FeS/Fe_3C@N-S-C-800 catalysts were specially treated with 10% hydrochloric acid solution for 12 h to obtain the catalyst FeS/Fe_3C@N-S-C-800-HCl. The XRD patterns of FeS/Fe_3C@N-S-C-800-HCl revealed the weaker peak intensity of FeS and Fe_3C nanoparticles (Figure S9, Supporting Information), which point out that a part of FeS@Fe_3C nanoparticles in the catalysts were etched-off after undergoing acid-leaching. The results of electrochemical activity investigation for ORR, OER, and HER in **Figures** 6B,E, 8A,C, and **10** show that the catalytic activity of FeS/Fe_3C@N-S-C-*n* is obviously higher than those over the catalysts without FeS/Fe_3C (N-S-C-800) and catalyst FeS/Fe_3C@N-S-C-800-HCl, which clearly testify that catalytic activity of FeS/Fe_3C@N-S-C-*n* for ORR, OER, and HER originates from the introduction of FeS/Fe_3C in N-S-codoped carbons. In the meantime, it was found that FeS has highly hydrophilicity and accelerates the adsorptions of aqueous substrates (O_2, H_2O, OH^-, or H^+),[97] but FeS delivers sluggish ORR kinetic process and has little catalytic activity for OER and HER due to the intrinsic low activity[97,98] and Fe/Fe_3C could assist the stabilization of the peroxide intermediate, promote a 4e⁻ ORR process and exhibits the preferable catalytic activity toward OER and HER,[99–101]but is insufficient toward O_2 adsorption.[84] In the prepared catalysts, FeS/Fe_3C@N-S-C-*n*,

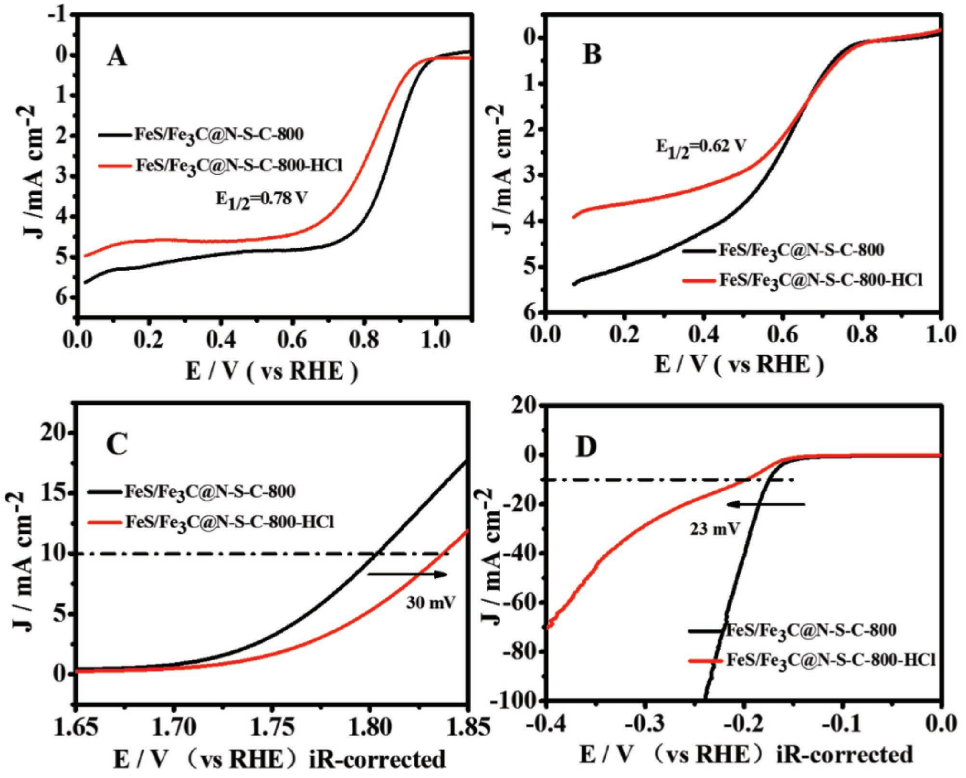

Figure 10. LSV curves of FeS/Fe$_3$C@N-S-C-800 and FeS/Fe$_3$C@N-S-C-800-HCl in A) 0.1 M KOH solution and B) 0.1 M HClO$_4$ solution for ORR. LSV curves of FeS/Fe$_3$C@N-S-C-800 and FeS/Fe$_3$C@N-S-C-800-HCl in C) 1 M KOH solution for OER and D) 0.5 M H$_2$SO$_4$ solution for HER.

FeS, and Fe$_3$C composite nanoparticles as a coupling body embedding in N-S-codoped carbons catalyst (FeS/Fe$_3$C@N-S-C). In the procedure of ORR over FeS/Fe$_3$C@N-S-C-*n*, FeS may improve the adsorption capacity of the catalyst for oxygen and raise the reactive rate of the direct four-electron reduction pathway from O$_2$ to H$_2$O catalyzed by Fe$_3$C, thus endowing FeS/Fe$_3$C@N-S-C-*n* with excellent catalytic performance. In the process of OER and HER over FeS/Fe$_3$C@N-S-C-*n*, FeS could promote the adsorptions capacity of the catalyst for aqueous substrates (H$_2$O, OH$^-$, or H$^+$) and facilitate reactants contact with the catalytic active sites Fe$_3$C, which would be helpful to accelerate the rate-determining reaction steps, thereby boosting the catalytic performance of FeS/Fe$_3$C@N-S-C-*n* for OER and HER. All this being said, Fe-related species (Fe$_3$C and FeS) could synergistically enhance the electrocatalytic activity of the FeS/Fe$_3$C@N-S-C-*n* for ORR, OER, and HER. Among them, Fe$_3$C is the initiator of catalytic activity and FeS is a synergistic cocatalyst.

3. Conclusion

Novel porous phenanthroline-based covalent organic frameworks with open metal-chelate sites were constructed using rigid building blocks. The metal implant of this Phen-COFs was achieved in DMSO solvent, which made Fe-DMSO coordination complexes involving in the Phen-COFs. The thermal conversion of this special COFs results into the formation of N-S-codoping carbons with embedded core–shell Fe$_3$C and FeS nanostructures. Impressively, the optimized FeS/Fe$_3$C@N-S-C-800 not only exhibited high-efficient ORR catalytic activity in acidic ($E_{1/2}$ = 0.64 V) and basic conditions ($E_{1/2}$ = 0.87 V), but also show higher activities for HER and OER. At the same time, the investigation results demonstrate that the FeS/Fe$_3$C@N-S-C materials possess trifunctional electrocatalytic activity (ORR, OER, HER) within a wide pH range from acidic to basic conditions. The synergistic interaction between FeS and Fe$_3$C nanoparticles embedded in N-S-codoped carbon surface contributed to such effective trifunctional electrocatalytic performance. Furthermore, a primary zinc–air battery by using the as-prepared FeS/Fe$_3$C@N-S-C-800 composite as the air cathode exhibited a remarkable peak power density and durability superior to those of its counterpart with the reference Pt/C air cathode. The strategy of rational design and orientated derivative provide a feasible route for preparing high-efficiency multifunctional electrocatalytic materials with inorganic nanoparticles composite to respond to the target electrocatalytic reactions in a wide range of PH. The prepared FeS/Fe$_3$C@N-S-C-800 could be a promising catalyst toward the new renewable energy technologies.

4. Experimental Section

Reagents and Chemicals: All chemicals were purchased from Sinopharm Group Chemical Reagent Co., Ltd. and used without further purification.

Synthesis of Covalent Phenanthroline Frameworks: 3, 8-Dibromophenanthroline (0.676 g, 2 mmol) and BTA (0.456 g, 2 mmol) were dissolved into a mixed solvent of tetrahydrofuran (THF) and *N*,*N*-

dimethylformamide (DMF) (V_{THF}/V_{DMF} = 2:1) in three-necked flask. The saturated solution of Na_2CO_3 (30 mL) and tetrakis(triphenylphosphine) palladium (0) (0.08 g, 0.07 mmol) were then added, and the resulting mixture was stirred and refluxed at 80 °C for 12 h in a flowing nitrogen atmosphere. After the reaction system above cooled to room temperature, an ammonia solution (15 mL, 5 wt%) was added and stirred for 15 min. A yellowish solid was collected by filtrating and washing with deionized water. The final Phen-COFs were obtained after being dried in vacuum at 60 °C.

To obtain iron-coordinated phenanthroline polymer (Fe-Phen-COFs), the above-prepared Phen-COFs (0.3 g) and Iron (II) acetate (1.2 g) were dissolved together in 30 mL of DMSO. Then, the resulting mixture was stirred and refluxed at 80 °C for 12 h under flowing nitrogen. A large amount of ethanol was added to the cooled reaction mixtures. The precipitation was collected and dried in vacuo to give a brown solid of Fe-Phen-COFs.

Synthesis of FeS/Fe$_3$C@N-S-C: The Fe-Phen-COFs products were pyrolyzed at 700–900 °C for 4 h in a quartz tube furnace under nitrogen atmosphere, with a heating rate of 2 °C min^{-1}. The prepared samples were marked as FeS/Fe_3C@N-S-C-*n* (*n* is the thermal-treatment temperature). For comparison, the FeS/Fe_3C@N-S-C-800 was leached in 10% of HCl solution for 12 h to give FeS/Fe_3C@N-S-C-800-HCl sample. The catalysts without FeS/Fe_3C (N-S-C-800) were prepared by paralyzing the dried mixture of Phen-COFs and DMSO at 800 °C for 4 h in a quartz tube furnace under nitrogen atmosphere.

Characterization: The XRD was performed on a D8 Advance X-ray diffractometer (Bruker AXS, Germany) with Cu Kα radiation (40 kV, 40 mA). The morphology and microstructure of samples were characterized by SEM (Hitachi ST-4800) and TEM (JEM-2010) with an acceleration voltage of 200 kV. The HAADF-STEM was carried out using JEM-2100F TEM (LVEM5, Japan). The chemical bonding states of samples were analyzed by XPS with Al Kα radiation (15 kV, 150 W) carried out on Axis Ultra DLD, and the C 1s (*BE* = 284.8 eV) as a reference to perform spectrum calibration. N_2 adsorption/desorption measurements were measured at 77 K in the Micromeritics ASAP 2020 analyzer. Measurement of Raman spectra of the samples was performed on a GX-PT-1500 (150) instrument with a 532 nm excitation laser (1 mW). Solid-state ^{13}C NMR spectra were measured at ambient temperature on a Bruker AVANCE III 400 MHz spectrometer. Room temperature UV–visible diffuse reflectance spectra were conducted on a Shimadzu UV 2401 PC with an integrating sphere attachment. The chemical structure of the samples was analyzed by the Fourier transform infrared spectra (Bruker Tensor 27) in KBr pellets.

XAFS Measurement: The X-ray absorption find structure spectra (Fe K-edge) were collected at 1W1B station in Beijing Synchrotron Radiation Facility (BSRF), China. The storage rings of BSRF were operated at 2.5 GeV with a maximum current of 250 mA. Using Si (111) double-crystal monochromator, the data collection was carried out in transmission mode using ionization chamber. All XAS spectra were recorded in room conditions in fluorescence mode.

XAFS Analysis and Results: The acquired EXAFS data were processed according to the standard procedures using the ATHENA module implemented in the IFEFFIT software packages.[102] The k^3-weighted EXAFS spectra were obtained by subtracting the postedge background from the overall absorption and then normalizing with respect to the edge-jump step. Subsequently, k^3-weighted $\chi(k)$ data of Cu K-edge were Fourier transformed to real (R) space using Hanning windows (dk = 1.0 Å^{-1}) to separate the EXAFS contributions from different coordination shells. To obtain the quantitative structural parameters around central atoms, least-squares curve parameter fitting was performed using the ARTEMIS module of IFEFFIT software packages.[103]

^{57}Fe Mössbauer spectra were recorded at room temperature using a Wissel accelerated Mossbauer spectrometer with a proportional counter. Moving ^{57}Co (Pd) in a constant acceleration mode was used as the radioactive source. The spectrum was fitted with a combination of Lorentzian lines.

Electrochemical Measurement: The electrocatalytic properties (ORR, OER, HER) of the as-prepared catalysts were characterized in a three-electrode system by CV, RDE techniques, and ring disk electrode (RRDE) techniques on the CHI-760C electrochemical analyzer. A glassy carbon disk electrode (5 mm in diameter, Pine) or a glassy carbon RRDE (5.6 mm in diameter, Pine) was used as the working electrode. An Ag/AgCl electrode (KCl, 3 M) was employed as reference electrode. The counter electrode was a Pt wire in the ORR and OER measurement or a graphite rod in the HER. The catalyst ink was prepared by ultrasonically dispersing 10 mg of catalyst in a solution containing 1.28 mL of ethanol containing 30 µL Nafion (5 wt%) solution to form a homogeneous suspension. Then, a little of catalyst ink was pipetted onto the surface of the polished glassy carbon electrode and dried at room temperature.

The electrocatalytic properties for ORR in alkaline electrolytes were carried out in O_2 saturated 0.1 M KOH solution and the potential range from −1.2 and +0.2 V (vs Ag/AgCl) at a scan rate of 5 mV s^{-1} at the ambient temperature. Acid tests were studied in O_2 saturated 0.1 M $HClO_4$ solution and the potential range was between 1.0 and −0.2 V (vs Ag/AgCl). Neutral tests were studied in O_2 saturated 0.01 M PBS solution and the potential range was between −1.0 and 0.4 V (vs Ag/AgCl). The general loading of FeS/Fe_3C@N-C-*n* samples on the working electrode was 0.3 mg cm^{-2} in 0.1 M KOH and 0.01 M PBS electrolytes and 0.6 mg cm^{-2} in 0.1 M $HClO_4$ solution. The catalyst loading of Pt/C (JM) was 0.1 mg cm^{-2} on the electrode in both electrolytes for comparison. All the potentials here were referenced to the reversible hydrogen electrode (RHE) potentials. The kinetic parameters have been calculated by Koutecky–Levich (K-L) equations[104]

$$\frac{1}{J} = \frac{1}{J_L} + \frac{1}{J_K} = \frac{1}{B\omega^{1/2}} + \frac{1}{J_K} \tag{1}$$

$$B = 0.62\, nFC_0 \left(D_0\right)^{2/3} \gamma^{-1/6} \tag{2}$$

$$J_K = nFkC_0 \tag{3}$$

in which J, J_K, and J_L are the measured current density, kinetic and diffusion-limiting current densities, respectively; ω is the angular velocity of the disk, n is the number of electrons transferred in ORR, F is the Faraday constant (F = 96 485 C mol L^{-1}), C_0 is the bulk solubility of O_2, D_0 is diffusion coefficient of O_2, γ is the kinematic viscosity of the electrolyte, and k is the electron transfer rate constant. The number of electrons transferred (n) can be obtained from the slope of the K-L plots.

Linear sweep voltammetry (LSV) for OER and HER were conducted with a scan rate of 5 mV s^{-1} in 1.0 M KOH, 0.01 M PBS, and 0.5 M H_2SO_4 solutions at room temperature, where graphite rod was employed as the counter for HER measurements. The general loading of catalysts in the OER and HER on the working electrode was 0.6 mg cm^{-2}. The iR-compensation was performed by electrochemical impedance spectroscopy to correct the compensated potential. The LSV curves were replotted as overpotential (η) versus log current (log j) to get Tafel plots for quantification of the OER and HER kinetic performance of as-prepared catalysts. By fitting the linear part of the Tafel plots to obtain the Tafel slope (b) according to the Tafel equation ($\eta = a + b \log(j)$).

Zinc–Air Batteries: Rechargeable zinc–air batteries in a two-electrode system were assembled according to the following procedures.[105] The air cathode was prepared by loading the catalyst (with a loading of 4 mg cm^{-2}) onto a carbon cloth substrate. A polished Zn foil was applied as the anode, and 6 M KOH filled with 0.2 M $Zn(Ac)_2$ was applied as the electrolyte to form zincate ($Zn(OH)_4^{2-}$) to ensure reversible Zn electrochemical reactions at the anode. The discharge polarization and power density plots were recorded using a galvanodynamic method. Galvanostatic discharge–charge cycling curves were performed at room temperature, in which one cycle consists of one discharge step followed by one charge step of the same current density and duration time (20 mA cm^{-2} for 24 h with a 10 min cycling).

Supporting Information

Supporting Information is available from the Wiley Online Library or from the author.

Acknowledgements

The authors are grateful for financial support from the China National Natural Science Foundation (No. 21303058), the Shanghai Municipal Natural Science Foundation (No. 13ZR1412400), and the key project of Shanghai Science and Technology Committee (No. 14231200300). The authors are thankful to the beamline 1W1B-XAFS station of Beijing Synchrotron Radiation Facility (BSRF) for XAS measurements.

Conflict of Interest

The authors declare no conflict of interest.

Keywords

carbon, covalent phenanthroline frameworks, FeS@Fe$_3$C, Pt-free catalysts, trifunctional electrocatalysts

Received: June 9, 2018
Revised: October 3, 2018
Published online:

---

[1] M. Zhou, Y. Xu, Y. Lei, *Nano Today* **2018**, *20*, 33.
[2] H. W. Liang, X. D. Zhuang, S. Bruller, X. L. Feng, K. Mullen, *Nat. Commun.* **2014**, *5*, 4973.
[3] I. S. Amiinu, X. B. Liu, Z. H. Pu, W. Q. Li, Q. D. Li, J. Zhang, H. L. Tang, H. N. Zhang, S. C. Mu, *Adv. Funct. Mater.* **2018**, *28*, 1704638.
[4] H. P. Zhao, M. Zhou, L. Y. Wen, Y. Lei, *Nano Energy* **2015**, *13*, 790.
[5] L. L. Z, J. Xiao, H. Y. Wang, M. H. Shao, *ACS Catal.* **2017**, *7*, 7855.
[6] S. Dutta, A. Bhaumik, K. C. W. Wu, *Energy Environ. Sci.* **2014**, *7*, 3574.
[7] Y. J. Tang, M. R. Gao, C. H. Liu, S. L. Li, H. L. Jiang, Y. Q. Lan, M. Han, S. H. Yu, *Angew. Chem., Int. Ed.* **2015**, *54*, 12928.
[8] Y. Nie, L. Li, Z. Wei, *Chem. Soc. Rev.* **2015**, *44*, 2168.
[9] Y. Jiao, Y. Zheng, M. Jaroniec, S. Z. Qiao, *Chem. Soc. Rev.* **2015**, *44*, 2060.
[10] J. Bao, X. D. Zhang, B. Fan, J. J. Zhang, M. Zhou, W. L. Yang, X. Hu, H. Wang, B. C. Pan, Y. Xie, *Angew. Chem.* **2015**, *127*, 7507.
[11] G. S. Hutchings, Y. Zhang, J. Li, B. T. Yonemoto, X. Zhou, K. Zhu, F. Jiao, *J. Am. Chem. Soc.* **2015**, *137*, 4223.
[12] S. Chen, J. Bi, Y. Zhao, L. Yang, C. Zhang, Y. Ma, Q. Wu, X. Wang, Z. Hu, *Adv. Mater.* **2012**, *24*, 5593.
[13] J. Zhang, Z. Zhao, Z. Xia, L. Dai, *Nat. Nanotechnol.* **2015**, *10*, 444.
[14] Q. Li, R. Cao, J. Cho, G. Wu, *Adv. Energy Mater.* **2014**, *4*, 1301415.
[15] J. Wang, K. Li, H. Zhong, D. Xu, Z. Wang, Z. Jiang, Z. Wu, X. Zhang, *Angew. Chem., Int. Ed.* **2015**, *54*, 10530.
[16] H. Wang, Z. Lu, D. Kong, J. Sun, T. M. Hymel, Y. Cui, *ACS Nano* **2014**, *8*, 4940.
[17] Y. P. Zhu, Y. P. Liu, T. Z. Ren, Z. Y. Yuan, *Adv. Funct. Mater.* **2015**, *25*, 7337.
[18] J. Zhang, L. Qu, G. Shi, J. Liu, J. Chen, L. Dai, *Angew. Chem.* **2016**, *128*, 2270.
[19] L. Zhuang, L. Ge, Y. Yang, M. Li, Y. Jia, X. Yao, Z. Zhu, *Adv. Mater.* **2017**, *29*, 1606793.
[20] Y. Ping, R. J. Nielsen, W. A. Goddard, *J. Am. Chem. Soc.* **2017**, *139*, 149.
[21] C. Hu, L. Dai, *Adv. Mater.* **2017**, *29*, 1604942.
[22] Y. Jia, L. Zhang, G. Gao, H. Chen, B. Wang, J. Zhou, M. T. Soo, M. Hong, X. Yan, G. Qian, *Adv. Mater.* **2017**, *29*, 1700017.
[23] J. Zhang, L. Dai, *Angew. Chem.* **2016**, *128*, 13490.
[24] L. Shang, H. Yu, X. Huang, T. Bian, R. Shi, Y. Zhao, G. I. N. Waterhouse, L. Z. Wu, C. H. Tung, T. Zhang, *Adv. Mater.* **2016**, *28*, 1668.
[25] F. L. Meng, Z. L. Wang, H. X. Zhong, J. Wang, J. M. Yan, X. B. Zhang, *Adv. Mater.* **2016**, *28*, 7948.
[26] X. Cui, S. Yang, X. Yan, J. Leng, S. Shuang, P. M. Ajayan, Z. Zhang, *Adv. Funct. Mater.* **2016**, *26*, 5708.
[27] C. Lv, Q. Yang, Q. Huang, Z. Huang, H. Xia, C. Zhang, *J. Mater. Chem. A* **2016**, *4*, 13336.
[28] S. Fu, C. Zhu, J. Song, M. H. Engelhard, X. Li, D. Du, Y. Lin, *ACS Energy Lett.* **2016**, *1*, 792.
[29] H. W. Liang, W. Wei, Z. S. Wu, X. L. Feng, K. Müllen, *J. Am. Chem. Soc.* **2013**, *135*, 16002.
[30] Q. P. Lin, X. H. Bu, A. G. Kong, C. Y. Mao, X. Zhao, F. Bu, P. Y. Feng, *J. Am. Chem. Soc.* **2015**, *137*, 2235.
[31] Y. Hu, J. O. Jensen, W. Zhang, S. Martin, R. Chenitz, C. Pan, W. Xing, N. J. Bjerrum, Q. F. Li, *J. Mater. Chem. A* **2015**, *3*, 1752.
[32] Y. Hu, J. O. Jensen, W. Zhang, L. N. Cleemann, W. Xing, N. J. Bjerrum, Q. Li, *Angew. Chem., Int. Ed.* **2014**, *53*, 3675.
[33] J. P. Dodelet, R. Chenitz, L. Yang, M. Lefevre, *ChemCatChem* **2014**, *7*, 1866.
[34] Y. Hou, T. Z. Huang, Z. H. Wen, S. Mao, S. M. Cui, J. H. Chen, *Adv. Energy Mater.* **2014**, *4*, 1400337.
[35] Z. H. Wen, S. Q. Ci, F. Zhang, X. L. Feng, S. M. Cui, S. Mao, S. L. Luo, Z. He, J. H. Chen, *Adv. Mater.* **2012**, *24*, 1399.
[36] C. Giordano, A. Kraupner, I. Fleischer, C. Henrich, G. Klingelhöfer, M. Antonietti. *J. Mater. Chem.* **2011**, *21*, 16963.
[37] X. Fan, Z. Peng, R. Ye, H. Zhou, X. Guo, *ACS Nano* **2015**, *9*, 7407.
[38] J. S. Lee, G. S. Park, S. T. Kim, M. Liu, J. Cho, *Angew. Chem.* **2013**, *125*, 1060.
[39] W. Yang, X. Liu, X. Yue, J. Jia, S. Guo, *J. Am. Chem. Soc.* **2015**, *137*, 1436.
[40] B. K. Barman, K. K. Nanda, *Green Chem.* **2016**, *18*, 427.
[41] Y. Sun, C. Liu, D. C. Grauer, J. Yano, J. R. Long, P. Yang, C. J. Chang, *J. Am. Chem. Soc.* **2013**, *135*, 17699.
[42] N. Wang, L. G. Li, D. K. Zhao, X. W. Kang, Z. H. Tang, S. W. Chen, *Small* **2017**, *13*, 1701025.
[43] S. Wang, S. Dou, L. Tao, J. Huo, L. Dai, *Energy Environ. Sci.* **2016**, *9*, 1320.
[44] X. Cao, X. Zheng, J. Tian, C. Jin, K. Ke, R. Yang, *Electrochim. Acta* **2016**, *191*, 776.
[45] P. Ganesan, M. Prabu, J. Sanetuntikul, S. Shanmugam, *ACS Catal.* **2015**, *5*, 3625.
[46] J. Staszak-Jirkovský, C. D. Malliakas, P. P. Lopes, N. Danilovic, S. S. Kota, K. C. Chang, B. Genorio, D. Strmcnik, V. R. Stamenkovic, M. G. Kanatzidis, *Nat. Mater.* **2016**, *15*, 197.
[47] T. W. Lin, C. J. Liu, C. S. Dai, *Appl. Catal., B* **2014**, *154–155*, 213.
[48] W. Zhou, X. J. Wu, X. Cao, X. Huang, C. Tan, J. Tian, H. Liu, J. Wang, H. Zhang, *Energy Environ. Sci.* **2013**, *6*, 2921.
[49] T. Zhu, H. B. Wu, Y. Wang, R. Xu, X. W. D. Lou, *Adv. Energy Mater.* **2012**, *2*, 1497.
[50] C. B. Ouyang, X. Wang, C. Wang, X. X. Zhang, J. H. Wu, Z. L. Ma, S. Dou, S. Y. Wang, *Electrochim. Acta* **2015**, *174*, 297.
[51] D. U. Lee, P. Xu, Z. P. Cano, A. G. Kashkooli, M. G. Park, Z. Chen, *J. Mater. Chem. A* **2016**, *4*, 7107.
[52] W. Yan, Z. Yang, W. Bian, R. Yang, *Carbon* **2015**, *92*,74.
[53] S. Zhou, N. S. Liu, Z. Y. Wang, J. J. Zhao, *ACS Appl. Mater. Interfaces* **2017**, *9*, 22578.
[54] Z. H. Xiang, Y. H. Xue, D. P. Cao, L. Huang, J. F. Chen, L. M. Dai, *Angew. Chem., Int. Ed.* **2014**, *53*, 2433.
[55] Z. H. Xiang, D. P. Cao, *J. Mater. Chem. A* **2013**, *1*, 2691.
[56] Z. H. Xiang, X. Zhou, C. H. Zhou, S. Zhong, X. He, C. P. Qin, D. P. Cao, *J. Mater. Chem.* **2012**, *22*, 22663.
[57] Z. H. Xiang, D. P. Cao, L. Huang, J. L. Shui, M. Wang, L. M. Dai, *Adv. Mater.* **2014**, *26*, 3315.

[58] C. Y. Lin, L. P. Zhang, Z. H. Zhao, Z. H. Xia, *Adv. Mater.* **2017**, *29*, 1606635.
[59] X. F. Fan, F. T. Kong, A. G. Kong, A. L. Chen, Z. Q. Zhou, Y. K. Shan, *ACS Appl. Mater. Interfaces* **2017**, *9*, 32840.
[60] S. Rau, R. Fischer, M. Jäger, B. Schäfer, S. Meyer, G. Kreisel, H. Görls, M. Rudolf, W. Henry, J. G. Vos, *Eur. J. Inorg. Chem. 2004*, **2004**, 2001.
[61] F. Xu, B. Hu, T. Tao, W. Huang, *Struct. Chem.* **2011**, *22*, 123.
[62] V. Amani, N. Safari, B. Notash, H. R. Khavasi, *J. Coord. Chem.* **2009**, *62*, 1939.
[63] K. Nakamoto, Y. Morimoto, A. Martell, *J. Am. Chem. Soc.* **1961**, *83*, 4528.
[64] Y. Wang, X. T. Chen, Q. P. Lin, A. G. Kong, Q. G. Zhai, S. L. Xie, P. Y. Feng, *Nanoscale* **2017**, *9*, 862.
[65] C. C. Su, J. W. Faller, *Inorg. Chem.* **1974**, *13*, 1734.
[66] Z. S. Wu, L. Chen, J. Z. Liu, K. Parvez, H. H. Liang, J. Shu, H. Sachdev, R. Graf, X. L. Feng, K. Müllen, *Adv. Mater.* **2014**, *26*, 1450.
[67] W. Xia, A. Mahmood, Z. B. Liang, R. Q. Zou, S. J. Guo, *Angew. Chem., Int. Ed.* **2016**, *55*, 2650.
[68] C. T. We, C. T. Wei, M. X. Shen, K. L. Ai, L. H. Lu, *Carbon* **2017**, *123*, 135.
[69] A. G. Kong, X. F. Zhu, Z. Han, Y. Y. Yu, Y. B. Zhang, B. Dong, Y. K. Shan, *ACS Catal.* **2014**, *4*, 1793.
[70] Q. Zuo, P. P. Zhao, W. Luo, G. Z. Cheng, *Nanoscale* **2016**, *8*, 14271.
[71] Z. Pei, H. Li, Y. Huang, Q. Xue, Y. Huang, M. Zhu, Z. Wang, C. Zhi, *Energy Environ. Sci.* **2017**, *10*, 742.
[72] Z. X. Pei, Z. J. Tang, Z. X. Liu, Y. Huang, Y. K. Wang, H. F. Li, Q. Xue, M. S. Zhu, D. M. Tang, C. Y. Zhi, *J. Mater. Chem. A* **2018**, *6*, 489.
[73] C. Q. Li, C. S. He, F. Z. Sun, M. C. Wang, J. H. Wang, Y. Q. Lin, *ACS Appl. Nano Mater.* **2018**, *1*, 1801.
[74] D. A. Pyles, J. W. Crowe, L. A. Baldwin, P. L. McGrier, *ACS Macro Lett.* **2016**, *5*, 1055.
[75] A. G. Kong, Y. Y. Kong, X. F. Zhu, Z. Han, Y. K. Shan, *Carbon* **2014**, *78*, 49.
[76] G. Z. Shen, X. R. Sun, H. W. Zhang, Y. Liu, J. Zhang, A. Meka, L. Zhou, C. Z. Yu, *J. Mater. Chem. A* **2015**, *3*, 24041.
[77] K. Fominykh, P. Chernev, I. Zaharieva, J. Sicklinger, G. Stefanic, M. Döblinger, A. Müller, A. Pokharel, S. Böcklein, C. Scheu, T. Bein, *ACS Nano* **2015**, *9*, 5180.
[78] U. Y. Qazi, C. Z. Yuan, N. Ullah, Y. F. Jiang, M. Imran, A. Zeb, S. J. Zhao, R. Javaid, A. W. Xu, *ACS Appl. Mater. Interfaces* **2017**, *9*, 28627.
[79] A. Aijaz, J. Masa, C. Rçsler, H. Antoni, R. A. Fischer, W. Schuhmann, M. Muhler, *Chem. – Eur. J.* **2017**, *23*, 12125.
[80] W. Yang, L. Chen, X. Liu, X. Yue, C. Liu, J. Jia, *J. Mater. Chem. A* **2016**, *4*, 5834.
[81] X. X. Ma, Y. Su, X. Q. He, *Catal. Sci. Technol.* **2017**, *7*, 1181.
[82] Y. Li, F. Cheng, J. Zhang, Z. Chen, Q. Xu, S. Guo, *Small* **2016**, *12*, 2839.
[83] S. N. Bhange, S. M. Unni, S. Kurungot, *J. Mater. Chem. A* **2016**, *4*, 6014.
[84] K. Strickland, E. Miner, Q. Y. Jia, U. Tylus, N. Ramaswamy, W. T. Liang, M.-T. Sougrati, F. Jaouen, S. Mukerjee, *Nat. Commun.* **2015**, *6*, 7343.
[85] S. T. Stripp, G. Goldet, C. Brandmayr, O. Sanganas, K. A. Vincent, M. Haumann, F. A. Armstrong, T. Happe, *Proc. Natl. Acad. Sci. USA* **2009**, *106*, 17331.
[86] A. Serov, K. Artyushkova, E. Niangar, C. Wang, N. Dale, F. Jaouen, M.-T. Sougrati, Q. Y. Jia, S. Mukerjee, P. Atanassov, *Nano Energy* **2015**, *16*, 293.
[87] J. Jiang, S. Lu, H. Gao, X. Zhang, H. Q. Yu, *Nano Energy* **2016**, *27*, 526.
[88] B. Hua, M. Li, J. L. Luo, *Nano Energy* **2018**, *49*, 117.
[89] X. Zou, Y. P. Liu, G. D. Li, Y. Y. Wu, D. P. Liu, W. Li, H. W. Li, D. J. Wang, Y. Zhang, X. X. Zou, *Adv. Mater.* **2017**, *29*, 1700404.
[90] P. Z. Chen, T. P. Zhou, M. X. Zhang, Y. Tong, C. G. Zhong, N. Zhang, L. D. Zhang, C. Z. Wu, Y. Xie, *Adv. Mater.* **2017**, *29*, 1701584.
[91] J. S. Li, Y. J. Tang, C. H. Liu, S. L. Li, R. H. Li, L. Z. Dong, Z. H. Dai, J. C. Bao, Y. Q. Lan, *J. Mater. Chem. A* **2016**, *4*, 1202.
[92] L. L. Feng, G. D. Li, Y. P. Liu, Y. Y. Wu, H. Chen, Y. Wang, Y. C. Zou, D. J. Wang, X. X. Zou, *ACS Appl. Mater. Interfaces* **2015**, *7*, 980.
[93] J. Q. Chi, W. K. Gao, J. H. Lin, B. Dong, J. F. Qin, Z. Z. Liu, B. Liu, Y. M. Chai, C. G. Liu, *J. Catal.* **2018**, *360*, 9.
[94] H. L. Jiang, Y. H. Zhu, Q. Feng, Y. H. Su, X. L. Yang, C. Z. Li. *Chem. – Eur. J.* **2014**, *20*, 3106.
[95] Z. H. Xue, H. Su, Q. Y. Yu, B. Zhang, H. H. Wang, X. H. Li, J. S. Chen. *Adv. Energy Mater.* **2017**, *7*, 1602355.
[96] X. X. Zou, X. X. Huang, A. Goswami, R. Silva, B. R. Sathe, E. Mikmekov, T. Asefa. *Angew. Chem.* **2014**, *126*, 4461.
[97] M. X. Shen, C. P. Ruan, Y. Chen, C. H. Jiang, K. L. Ai, L. H. Lu, *ACS Appl. Mater. Interfaces* **2015**, *7*, 1207.
[98] X. X. Zou, Y. Y. Wu, Y. P. Liu, D. P. Liu, W. Li, L. Gu, H. Liu, P. W. Wang, L. Sun, Y. Zhang, *Chem* **2018**, *4*, 1139.
[99] Y. Zhang, J. T. Zai, K. He, X. F. Qian, *Chem. Commun.* **2018**, *54*, 3158.
[100] C. S. Song, S. K. Wu, X. P. Shen, X. L. Miao, Z. Y. Ji, A. H. Yuan, K. Q. Xu, M. M. Liu, X. L. Xie, L. R. Kong, G. X. Zhu, S. A. Shah, *J. Colloid Interface Sci.* **2018**, *524*, 93.
[101] H. Huang, X. Feng, C. C. Du, S. Y. Wu, W. B. Song, *J. Mater. Chem. A* **2015**, *3*, 4976.
[102] B. Ravel, M. Newville, *J. Synchrotron Radiat.* **2005**, *12*, 537.
[103] J. J. Rehr, R. C. Albers, *Rev. Mod. Phys.* **2000**, *72*, 621.
[104] W. Niu, L. Li, X. Liu, N. Wang, J. Liu, W. Zhou, Z. Tang, S. Chen, *J. Am. Chem. Soc.* **2015**, *137*, 5555.
[105] S. G. Wang, J. W. Qin, T. Meng, M. H. Cao, *Nano Energy* **2017**, *39*, 626.